ORIGINAL RESEARCH ARTICLE

Dimensional Effects of Hybrid Bond Layers on CFRP Metallized by Ti Cold Spray

Po-Lun Feng[1] · Kinal Kim[2] · Adolfo Blassino[3] · Isaac Nault[3] · Sang-Eui Lee[2] · Steven Nutt[1]

Abstract Hybrid bond layers (BLs) were designed, fabricated, and evaluated for cold spray metallization of CFRP. The bond layers consisted of metal mesh embedded in a polymer film adhesive co-cured to the CFRP. Efforts were devoted to identifying the critical opening ratio—i.e., the ratio of mesh opening size to powder diameter, for deposition of an adherent coating. Analysis of powder deposited at mesh openings show a transition from erosion (at a mesh opening ratio of 6.4) to mechanical interlocking and formation of a continuous coating with decreasing opening ratio. Selection of opening ratio yielded either (a) a grid of consolidated thin-walled deposits atop mesh wires separated by microchannel openings, or (b) densified coatings of cold-sprayed Ti. The effective opening ratio increased with increasing diameter ratio—i.e., the ratio of wire diameter to powder size, a consequence of eroded wire peripheries at shallow impact angles. These findings inform the design of future hybrid BLs, in concert with the selection of powder size, for cold spray metallization of CFRP.

Introduction

Adhesion of cold-sprayed (CS) deposits relies primarily on interactions between the impinging powder and the substrate surface. For dissimilar classes of materials, particularly brittle substrates, bond layers are often required to render substrates compatible to the deposition process and to promote adhesion. Incorporation of a bond layer is widespread and has enabled cold spray (Ref 1) and thermal spray metallization (Ref 2, 3) of thermoset composites. However, the adhesion of CS deposits to thermoset composites generally does not meet service requirements.

In the present study, hybrid bond layers comprised of woven wire meshes with select opening sizes were embedded in an epoxy film adhesive to address this shortfall. The objective of the work was to determine the effects of feature dimensions within the bond layer with respect to powder size on the metallization of carbon fiber reinforced polymer (CFRP) by cold spray. The relative dimensions of powder, wire, and mesh opening governed the CS metal deposition and affected adhesive strength. Judicious selection of dimensional parameters led to fabrication of strongly bonded deposits on thermoset composites.

Polymer metallization generally imparts erosion resistance, electrical and thermal conductivity, and biocompatibility, and can be accomplished through vapor phase deposition, electroless plating, and recently - cold spray (Ref 4). This solid-state material consolidation technique

✉ Po-Lun Feng
  brianfeng@alumni.usc.edu

✉ Sang-Eui Lee
  selee@inha.ac.kr

1 Department of Chemical Engineering and Materials Science, M.C. Gill Composites Center, University of Southern California, Los Angeles, CA, USA

2 Department of Mechanical Engineering, Inha University, Incheon 22212, Korea

3 Army Research Laboratory, Aberdeen Proving Ground, Aberdeen, MD, USA

affords high deposition rates at low cost without the risk of thermal damage to the substrate or the formation of undesirable phases. The *in situ* formation of mechanical interlocks between CS powder and the substrate can create adherent interfaces without pre-treatment. Additional surfaces for interlocking and metallic bonding can be introduced by incorporating a wire mesh within the hybrid bond layer. The approach of hybrid bond layers aligns with a general progression toward scalable, cost-effective, eco-friendly surface preparation to form mechanical interlocks essential to thick (mm) composite metallization where chemical bonding yields insufficient adhesion (Ref 4).

CS metallization of polymers and composites encompasses joining both continuous metal coatings and additively manufactured structures to the substrate (Ref 5-7). To prevent substrate erosion during deposition, sprayed powders are currently limited to relatively soft metals (e.g., Sn, Al, (Ref 1, 8-11), and metallized substrates generally have been thermoplastics (Ref 12-14). Additionally, the manufacturing resolution (minimum feature size) of CS is on the order of mm, which restricts the intricacy of additively manufactured parts (Ref 15). Both limitations are addressed in this work, which demonstrates the feasibility of cold spraying Ti onto hybrid bond layers with select mesh dimensions. Demonstration trials yielded continuous, dense, well-bonded deposits and vertical thin-walled grids separated by open microchannels.

Additive manufacturing by CS has been investigated to mitigate the processing difficulties inherent to highly reactive Ti, while limiting the defect formation and residual stresses associated with high-temperature processes. Studies on CS-Ti have primarily focused on pure Ti with few on Ti alloys (Ref 16). The primary applications of CS-Ti are protective coatings for resistance to wear and corrosion (Ref 17), biocompatible coatings (Ref 18), and additive manufacturing (Ref 19, 20). To satisfy service requirements, *in situ*, pre- and post-spray thermal and/or mechanical treatments have been implemented to strengthen CS-Ti. Grains can be refined by friction stir processing (Ref 21), and voids can be reduced by hot isostatic pressing (Ref 22, 23). Load-bearing and complex Ti structures with internal channels (Ref 24) have been fabricated through multi-step processes (Ref 16). These developments can overcome the shortcomings of fusion-based methods and broaden future applications of CS-Ti.

In the present work, we demonstrate an alternative process route to join Ti to thermoset composites in a single step. The process involves direct CS metallization of a composite featuring a hybrid bond layer comprised of metal mesh and epoxy, and the approach is widely applicable. The purpose of the bond layer is to "compatibilize" both process and material, and to promote adhesion. The effect of the reinforcing mesh within the bond layer was investigated, focusing on geometric features. The opening ratio, defined as the mesh opening size to powder diameter, strongly affected the depth and content of embedded powder at the mesh openings after cold spray deposition. The diameter ratio, defined as the wire diameter to powder diameter, led to select erosion of wire peripheries. The dependence of deposit continuity and adhesion on these parameters was identified and can guide the selection of BL and powder dimensions. The findings demonstrate the ability to tailor hybrid bond layers to the desired form of the deposit to the intended application.

Experimental Methods

Bond Layer Preparation and Cold Spray Deposition

Commercial purity Ti powder (CP Ti, D90 = 40 μm, 325 × 325 mesh) was cold sprayed onto a hybrid metal-polymer bond layer (BL) on the surface of a CFRP laminate (1.5 mm thick), comprised of ten plies (0/90) of pre-preg (Toray 2510, Toray Industries, Inc., Tokyo, Japan). Figure 1 illustrates the two types of bond layer substrates – embedded and supported mesh. The wire mesh was fully embedded in the film adhesive (Fig. 1a) or positioned atop and supported by the film adhesive (Fig. 1b). The hybrid bond layer (Fig. 1a) was reinforced with Al 5056 wire mesh (McMaster-Carr, Elmhurst, IL, USA) embedded in an epoxy film adhesive with Al filler (LOCTITE® EA 9658 AERO, Henkel, Düsseldorf, Germany). The bond layer and CFRP were co-cured in a vacuum-bag only (VBO) process following manufacturer's guidelines and detailed in a previous study (Ref 1). To decouple the effects of the film adhesive and the metal mesh on deposit adhesion, supported mesh (Fig. 1b) was also cold sprayed to investigate interactions between CP Ti powder and Al wire. Three mesh opening sizes – BL50, BL120, and BL200 - were investigated as described in Table 1. The substrates were cold sprayed with He at 200 °C, 2.76 MPa, raster speed of 400 m/s, and a stand-off distance of 25.4 mm using a VRC Gen III CS system (VRC Metal Systems, Rapid City, SD, USA). The mean powder velocity of 594 m/s was measured at the nozzle exit using a laser velocimetry system (HiWatch HR1 CS, Oseir, Tampere, Finland).

Microstructural Analysis and Lug Shear Test

The hybrid metal-polymer bond layer and the deposits were sectioned and ion polished (JEOL SM-09010, Tokyo, Japan) for SEM (Helios G4 PFIB UXe, Thermo Fisher Scientific, Waltham, MA, USA) imaging to analyze both plan and cross sections. The supported mesh was cold
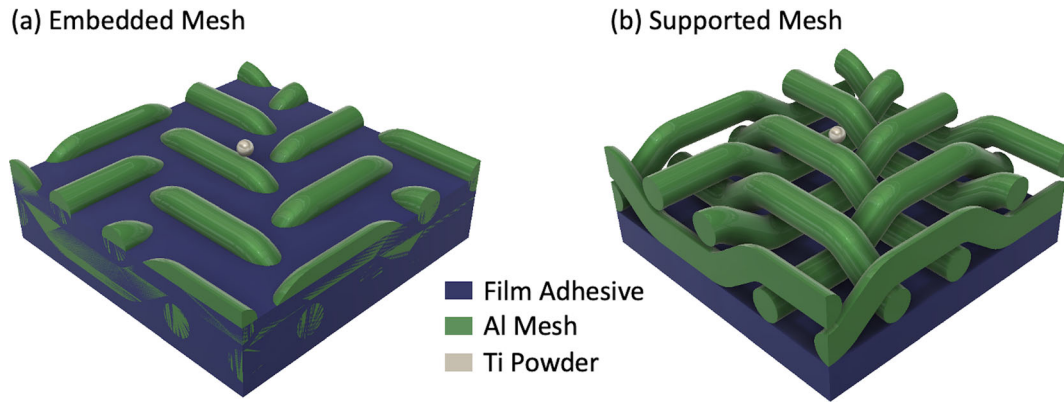
Fig. 1 Hybrid bond layer with (a) embedded mesh and (b) supported mesh

Table 1 Bond layer specifications

Bond Layer	Wire mesh	Mesh opening size (um)	Wire diameter (um)
BL50	50 × 50 Mesh	279.4	228.6
BL120	120 × 120 Mesh	109.2	101.6
BL200	200 × 200 Mesh	73.7	53.3

mounted before sectioning and polishing for cross-sectional imaging. EDS (Ultim Max, Oxford Instruments, Abingdon, UK) maps and line scans were used to detect the presence of Ti, Al, and O. The largest powder diameter − 44 μm, was used to calculate the opening ratio (mesh opening size to powder diameter) and the diameter ratio (wire diameter to powder diameter). Adhesive shear strength of the deposit (6-pass CP Ti followed by 30-pass CP Al) was measured according to MIL-J-24445A. The shear strength was calculated by taking the average of 5 measurements. The resulting fracture surfaces were examined by SEM to identify the adhesion mechanisms.

Finite Element Analysis

Two types of impact simulation were conducted, both with 2D thermo-mechanical coupling, using ABAQUS/Explicit with Lagrangian formulae. The first model simulated the impact of a single Ti particle onto supported mesh, as shown in Fig. 2(a). The wire mesh was positioned atop an epoxy substrate, and normal contact was defined between the surface of the wire mesh and the top surface of the epoxy. This simulation demonstrated wire erosion upon impact, as the position of impinging powder particle varied along the wire cross section. The second model simulated the impact of multiple Ti particles impinging onto BL120 and BL200, as shown in Fig. 2(b) and (c). This simulation depicted the impact load transferred to the wire mesh and the accumulation of CS powder at the mesh openings. In this simulation, all the particles traveled at the same impact velocity as the measured in-flight velocity. As shown in

Fig. 2, the particles were distributed in the same alternating grid arrangement for both BL120 and BL200 to reflect the different deposition behaviors on the bond layers. 38 particles in total accumulated to two particle layers for comparison with experimental results.

In both simulations, the Johnson-Cook (JC) model was used to simulate plasticity of the material. The erosion of epoxy in multiple particle impact was simulated using the Johnson-Cook damage criterion. The material parameters and properties used are listed in Table 2. The simulated impact velocity was 600 m/s, which was chosen based on the measured powder velocity (593.8 m/s), and the initial temperature was set to 298 K. The simulation grid size was $1/50d_p$ for single particle impact, and $1/20d_p$ for multiple particle impact. A coarser grid size was selected for the multiple particle simulations because of the larger computational resources compared to the single particle model. The element type was CPE4RT with reduced integration and hourglass control.

Results and Discussion

Microstructure

Figure 3 shows images of CS deposits produced with different bond layer designs. The images show that the continuity and structure of the deposit depended on the selected opening ratio (mesh opening size to powder diameter) and the pattern of the underlying mesh. An opening ratio of 6.4 (BL50) produced a discontinuous

Fig. 2 (a) Single particle impact simulation onto supported wire mesh. Multiple particle impact simulation of CS deposition onto (b) BL120 and (c) BL200
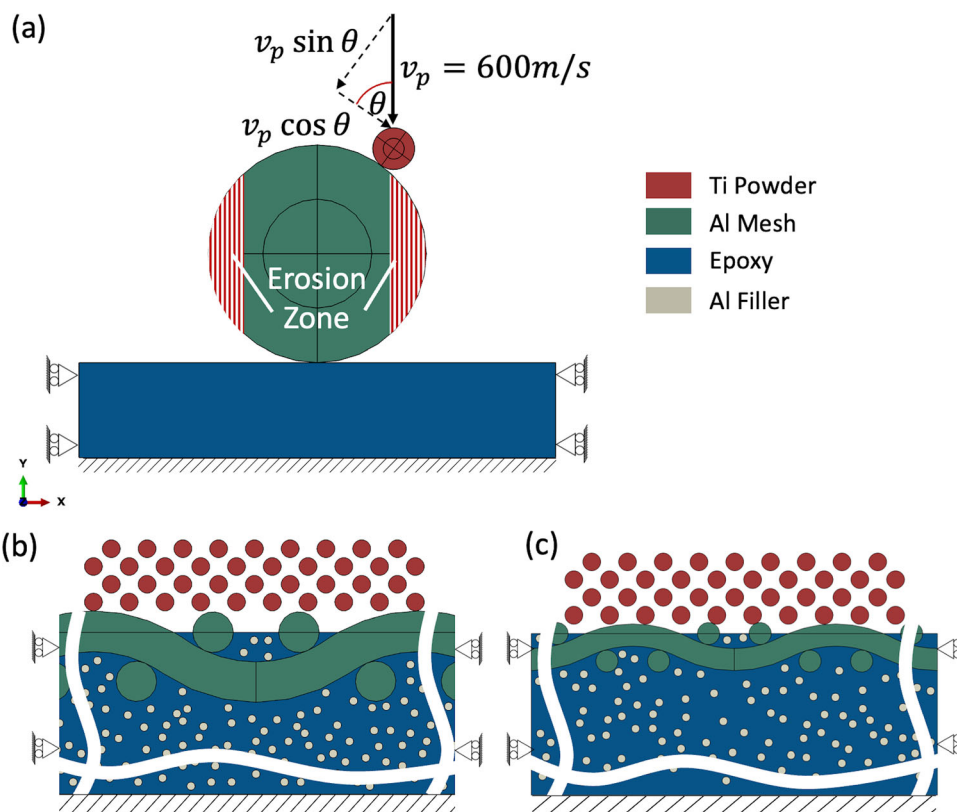

Table 2 Material properties for simulation

Material	Symbol	Unit	Pure Ti (Ref 46)	Al 5056 (Ref 47)	Epoxy (Ref 48)	Pure Al (Ref 27, 49)
Density	ρ	kg/m^3	4510	2640	1400	2710
Thermal conductivity	k	$W/m \cdot K$	16*	117	0.2	210
Specific heat	c_p	$J/kg \cdot K$	540	904	1000	904
Elasticity	Linear					
Young's modulus	E	GPa	116	71	2.8	68.9
Poisson's ratio	v	GPa	0.34	0.33	0.3	0.33
Plasticity	J-C Plasticity model					
Yield strength	A	MPa	806	140	89.77	148.4
Hardening coefficient	B	MPa	481	426	4200	345.5
Strain-hardening exponent	n	…	0.319	0.34	1.4	0.183
Strain rate constant	C	…	0.019	0.015	0.037	0.001
Softening constant	m	…	0.655	1	…	0.895
Melting temperature	T_m	K	1923	911	…	916
Reference temperature	T_r	K	298	300	…	293
Reference strain rate	$\dot{\epsilon_0}$	s^{-1}	1	1	0.0027	1
Damage criteria						
JC Damage	$d_1, d_2, d_3. d_4$		…	…	0.026, 0.05, 1.5, 0.028	…

structure (Fig. 3a and b), while a ratio of 1.7 (BL200) yielded a continuous coating (Fig. 3c and d). Figures 3(a) and (b) display vertically consolidated, thin-walled grid patterns with open microchannels on the 50×50 mesh. The sprayed microchannels replicated the weave topography of the mesh, and no excess powder
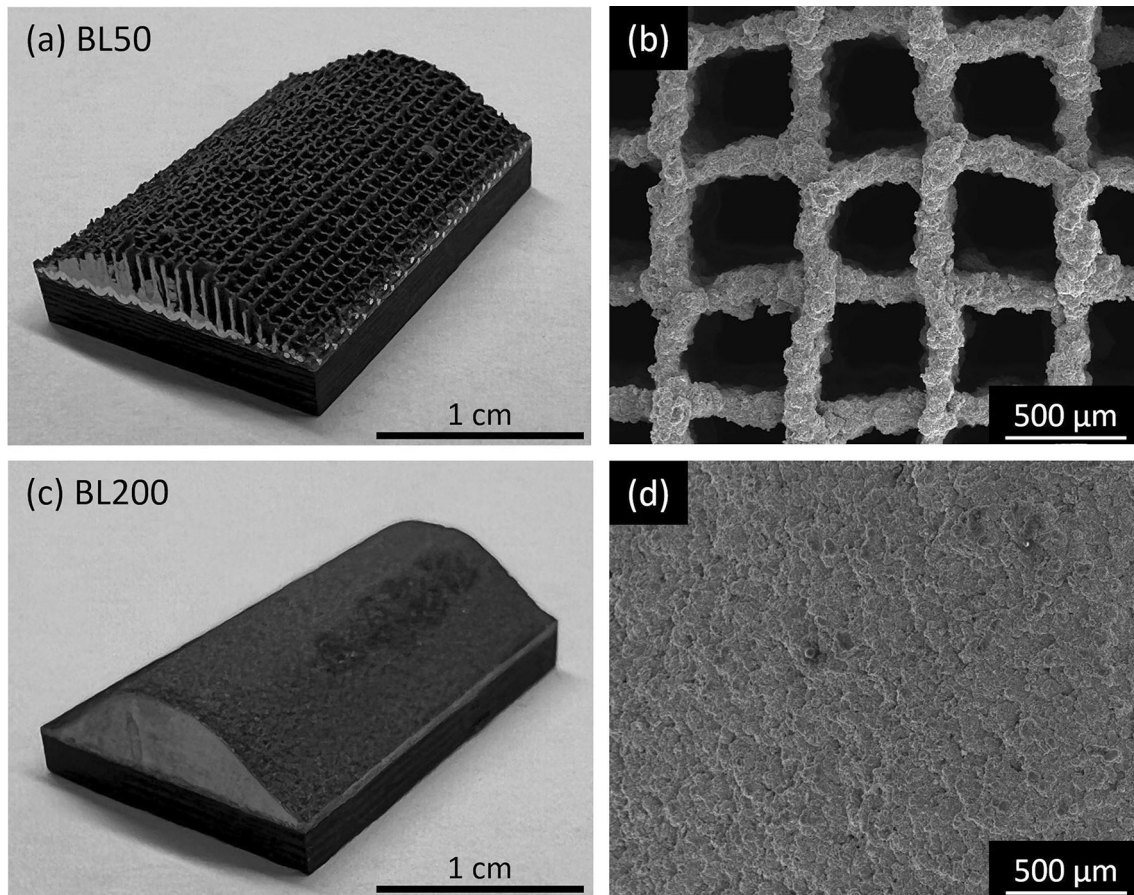
Fig. 3 36-pass deposit on (a) BL50 formed (b) thin-walled microchannels, while deposit on (c) BL200 formed a (d) continuous coating

fused to the sides of the walls. The finding indicates that the underlying mesh can serve as a template for additive manufacturing of upright micro-scale structures with thin walls ($\sim$ 150 um). This approach can overcome the current resolution limit of cold-sprayed features, which is on the order of mm (Ref 15). In contrast, Fig. 3(c) and (d) show a continuous and densified deposit on BL200. No porosity or cracks are evident in the plan view in Fig. 3(d). BL120, which is not shown here, spontaneously detached after cold spray because of weak deposit adhesion.

Images in Fig. 4 show deposition onto mesh wires and erosion of wire edges after 6-pass CS onto a supported 50 × 50 mesh (opening ratio: 6.4, diameter ratio: 5.2). The grid pattern of the wire was preserved, resulting in rectangular openings (Fig. 4a). The wire edges yielded no deposit and formed erosion zones at impact angles < 45° (calculated using Fig. 4(a) and (b). Figure 4(c) and (d) support this description and present a similar observation when the sample is viewed after tilting to 40°. The images display vertically stacked CP Ti powder at the center of the wires with steeply inclined sides. Powder consolidated only in the vertical direction, while no powder fused to the sides of the wire or deposit. Compared to the

6-pass deposit in Fig. 4(a), the wall spacing of the 36-pass deposit in Fig. 3(b) widened by $\sim$ 10% because of increased erosion of off-center deposits. The formation of a discontinuous structure was a function of both the opening ratio and the impact angle. The eroded regions of wires increased the effective opening ratio by widening the mesh opening required for powder to bridge and form a continuous deposit.

Figure 5 shows the deposition and degree of erosion of the wire at different impact angles. The total simulation time was 500 ns, and each image was captured immediately after the equivalent plastic strain (PEEQ) became constant over time. Deposition and erosion of the wire at a 90° spray angle depended on the local impact angle of impingement, as depicted in Fig. 5. Local impact angles greater than 45° led to cratered mesh wire around the impact site (Fig. 5a, b and c). However, impact angles *less* than or equal to 45° led to severe plastic deformation of the wire periphery, causing erosion (Fig. 5d, e, f). The velocity of the impinging particle can be decomposed into the normal component ($v_p\sin\theta$) and the tangential component ($v_p\cos\theta$), (shown previously in Fig. 2a). For impact sites at increasing distances from the wire center, the impact angle
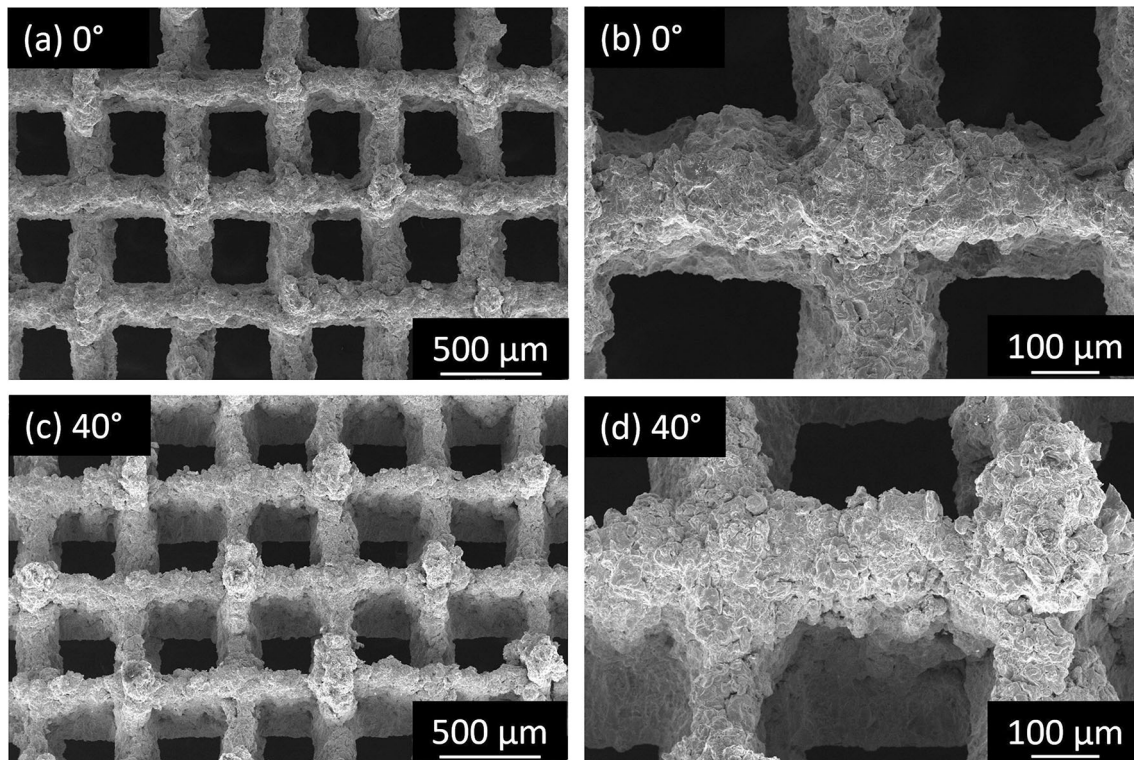
**Fig. 4** SE micrographs of 6-Pass CP Ti on supported 50 × 50 mesh at (a, b) 0° and (c, d) 40° tilt
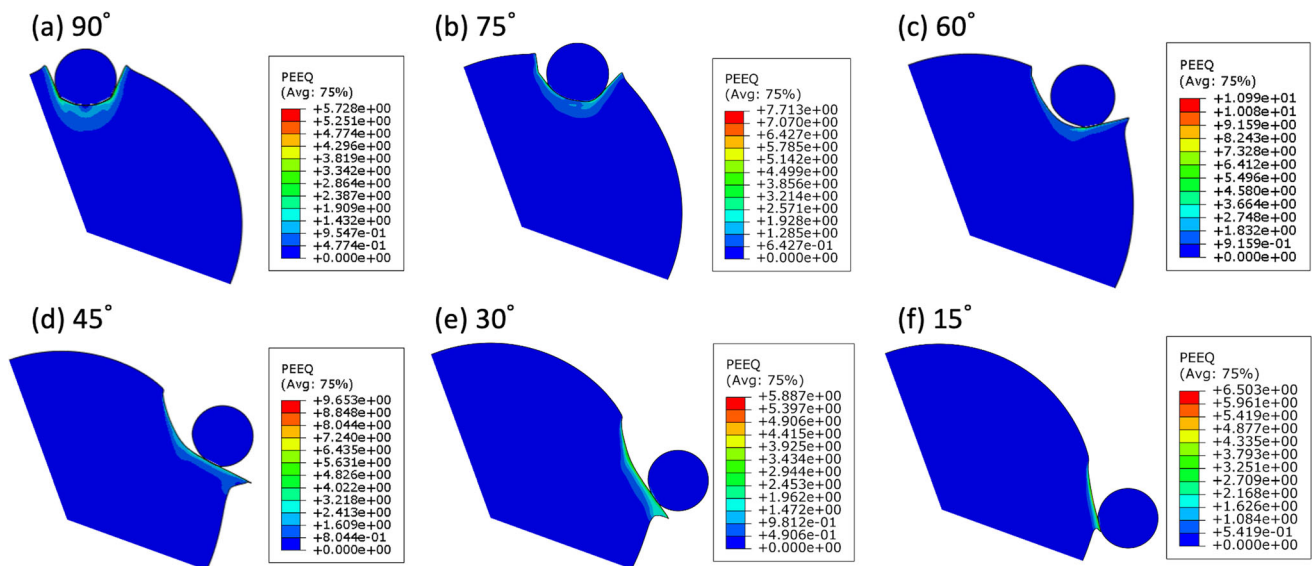
Fig. 5 FEA of single Ti particle impact on Al wire at (a) 90°, (b) 75°, (c) 60°, (d) 45°, (e) 30°, and (f) 15°

decreased. Correspondingly, the normal impact velocity reduced by a multiple of $\sin\theta$, reducing the crater depth and resulting in insufficient deformation for bonding. In concurrence, the tangential momentum elongated the crater and facilitated particle rebound. The progressively shorter crater rim failed to capture and retain subsequently impinging particles.

Similar conclusions can be drawn from analysis of the kinetic energy of the impinging particle, which transformed into friction dissipation, plastic dissipation, and recoverable strain energies (Ref 25, 26). A greater plastic dissipation energy (ALLPD variable in Abaqus) from the induced kinetic energy (ALLKE) correlated with the adhesion energy (Ref 27-29), i.e., the probability of particle

bonding to the substrate (Ref 26). Temporal evolution of plastic dissipation energy based on simulated impact angles are compared in Fig. 6. Plastic dissipation energy decreased in conjunction with the impact angle. At impact angles less than 45°, the plastic dissipation energy was less.
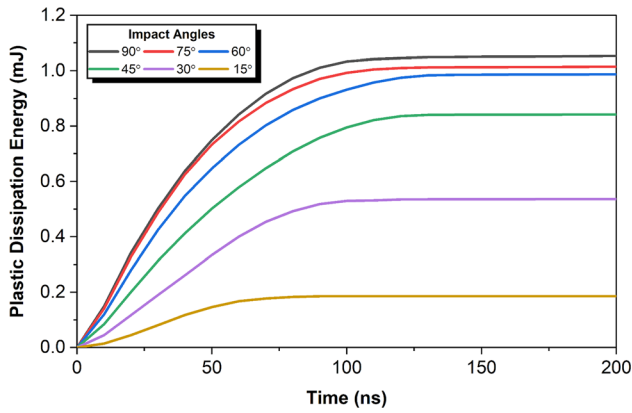

Fig. 6 Temporal evolution of plastic dissipation energy (ALLPD) at various impact angles

These findings were consistent with studies where impact angles less than 45-60° for various material combinations yielded negligible deposition (Ref 30-34).

Figure 7 shows bridging of wire openings and deposition onto film adhesive with 6-pass CS onto supported 120 × 120 mesh (opening ratio: 2.5). In the images in Fig. 7(a) and (b), over half of the 120 × 120 mesh openings are filled or partially covered by CP Ti powder (in contrast to those in Fig. 4, which showed consolidated powder only on the 50 × 50 mesh wires). The bridging of consolidated powder over wires at an elevation ∼ 150 μm above the mesh is shown in cross-section in Fig. 7(c). Within the deposit, porosity was present primarily above the wire openings. Figure 7(d) shows CP Ti powder stacked on the film adhesive after traveling through 120 × 120 mesh openings. Tamping by subsequently impinging powder did not effectively fuse powder above the mesh to powder directly on the film adhesive. The observation indicates that for embedded BLs, deposit adhesion depended primarily on wire attachment to the BL matrix.
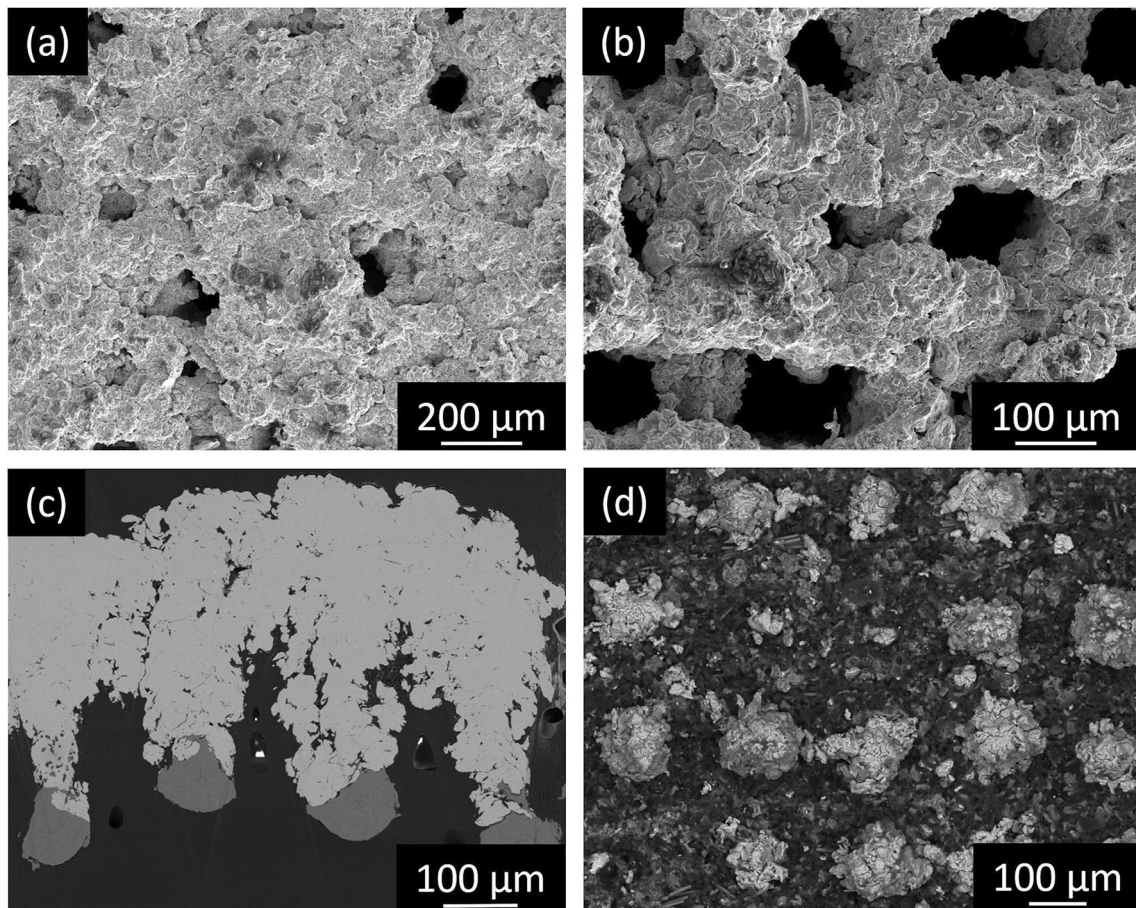
Fig. 7 SE micrographs of 6-Pass CP Ti on supported 120 × 120 mesh in (a, b) plan view, (c) cross section, and on the (d) underlying film adhesive in plan view
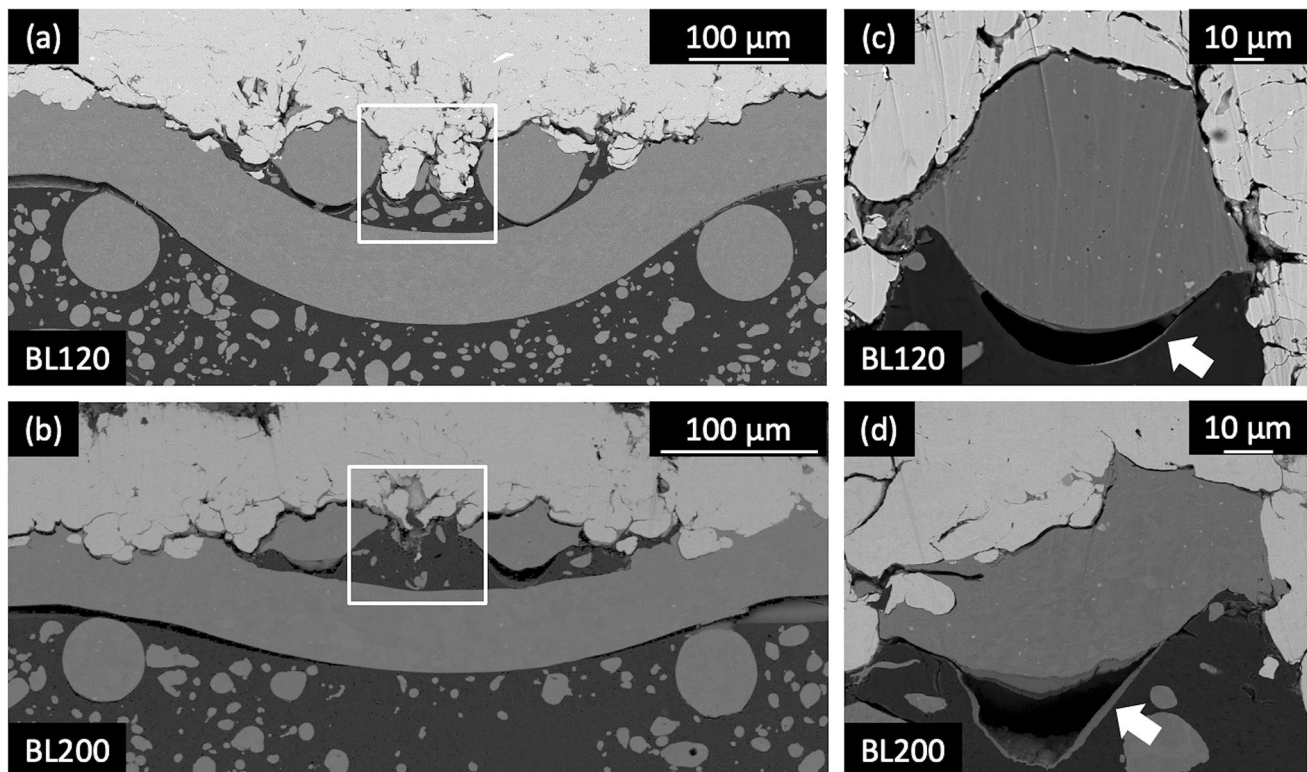
Fig. 8 BSE micrographs of Ti deposit on (a) BL120, (b) BL200 and wire separated from epoxy matrix in (c) BL120 and (d) BL200

Figure 8 shows the effects of opening ratio and diameter ratio on mechanical interlocking and wire separation in the hybrid bond layer. Figure 8(a) shows ~ 85 μm powder embedment in the area surrounded by three wires, framed in white. The sample (BL120, opening ratio 2.5), shows two parallel wires present top center, and one serpentine wire crossing beneath. In contrast, Figure 8(b) shows ~ 30 μm powder embedment in a similar region for BL200 (opening ratio 1.7). At the mesh opening, loosely bonded powder was observed (white frame), a result of detachment during sample preparation. The contribution of interlocking to adhesive strength would increase with embedment depth if the deposit extending into wire openings were fully consolidated, as demonstrated with CP Al in a previous study (Ref 1). However, the chosen CS parameters in this work yielded loosely bonded powder that was inadequately interlocked. For wires not in mutual contact, the separation distance from the epoxy matrix depended on the diameter ratio. Figures 8(c) and (d) show separation distances of 11 μm and 19 μm for diameter ratios of 2.3 and 1.2 (BL120 vs BL200).

The effect of opening ratio on mechanical interlocking was also demonstrated in multiple particle simulations shown in Fig. 9. The depth and content of powder embedment resembled the observations shown in Fig. 8. Under the same impact conditions, Ti powder penetrated more deeply into the opening of BL120 than BL200. In simulations, 1500 ns after impact, the residual stress generated in the Al wire exceeded the stress generated in the epoxy film adhesive. The stress distribution of both BL120 and BL200 indicated that the impact loads were transmitted primarily to the Al wire, mitigating the extent of epoxy erosion.

The consequence of load transfer between Al wire and epoxy resembles the direct impact of CS powder onto substrates. Figure 10(a) shows that only the wire nearer the surface interacted with CS-Ti and separated from the film adhesive. The separation between Al wires and epoxy was attributed to CTE mismatch and rebound kinetic energy after impact. Rebound of CS powder resulted in partial detachment and gap formation between the CS powder and the substrate (Ref 35, 36). Beneath the detached wire was a thin metal layer composed of oxidized Al and Ti as shown in Figures 10(b), (c), (d), (e) and (f) with EDS line scans and composition maps. This oxide layer was formed by the redeposition and oxidation of the sputtered Al and Ti during ion polishing of sample cross sections. Similar observations of ion beam-induced redeposition were reported elsewhere (Ref 37).

Shear strength measurements of BL200 (36.0 ± 3.0 MPa) revealed insights into the role of the wire mesh in adhesion, and provided context for assessing the suitability of the bond layer approach in practice. Figure 11 shows mixed mode failure between the CP Ti
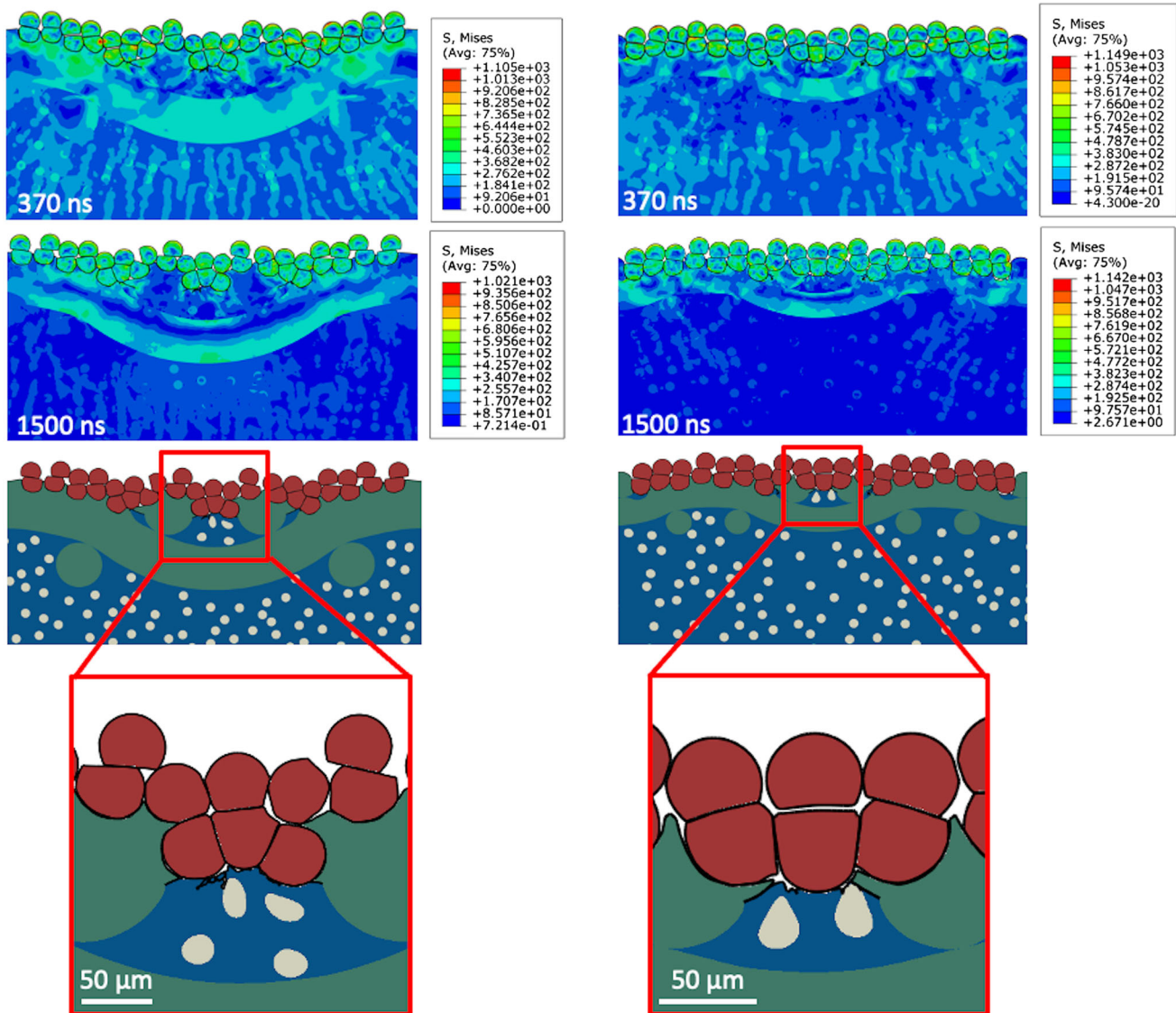
Fig. 9 Cross-section of simulated stress distribution of CS powder impinging (a) BL120 and (b) BL200

deposit and BL200 after shear tests. Figure 11(a) and (b) show regions of detached mesh, and bending and fracture of mesh wires on the substrate fracture surface. Figure 11(c) shows sparsely dispersed Ti powder (white, indicated by cyan arrows) that remained on the substrate fracture surface. Figure 11(d) shows detachment of Al wires (light grey, orange arrows) and Ti deposit (white, cyan arrows). Regions of the Ti deposit were interlocked with the film adhesive (dark grey), which was mixed with Al filler particles (light grey, orange arrows). The mixed failure mode indicated gradual crack propagation, and the failure mode undoubtedly contributed to fracture toughness. Both phenomena were dictated by the design of the hybrid bond layer.

In aerospace applications, the effectiveness of leading-edge protection by a metallic surface layer relies on the adhesion of the surface treatment as well as erosion mitigation in service. Poor adhesion even in a relatively small area can lead to entire debonding of leading-edge tapes (Ref 38). Erosion of leading edges can create surface asperities and trigger propagation of shear stress waves from the damage initiation site (Ref 38-40). In this work, the measured shear strength exceeded the overlap shear strength of a structural adhesive commonly used for aircraft maintenance and attaching leading-edge protection (33.8 MPa, Scotch-Weld AF 191 Film Adhesive (Ref 41)), (Ref 42-45). The hybrid bond layer also provided interlocking features that served as crack arresters at the
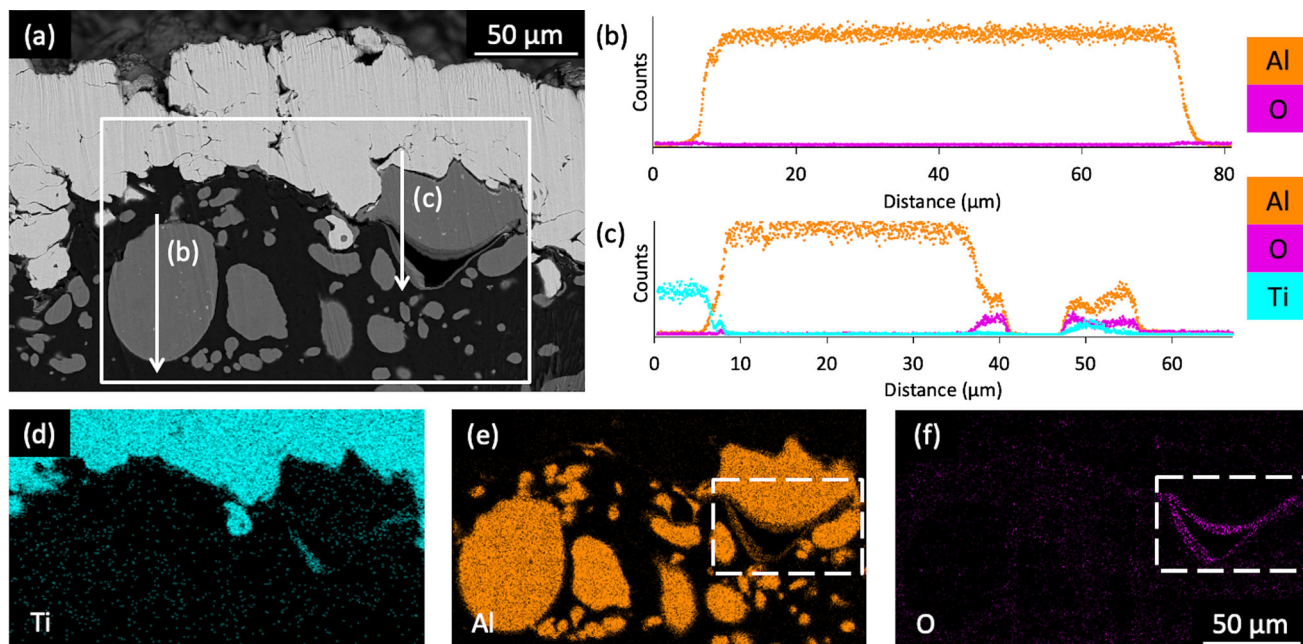
Fig. 10 (a) BSE micrograph of BL200 with EDS (b, c) line scans and (d-f) maps (outlined in (a))
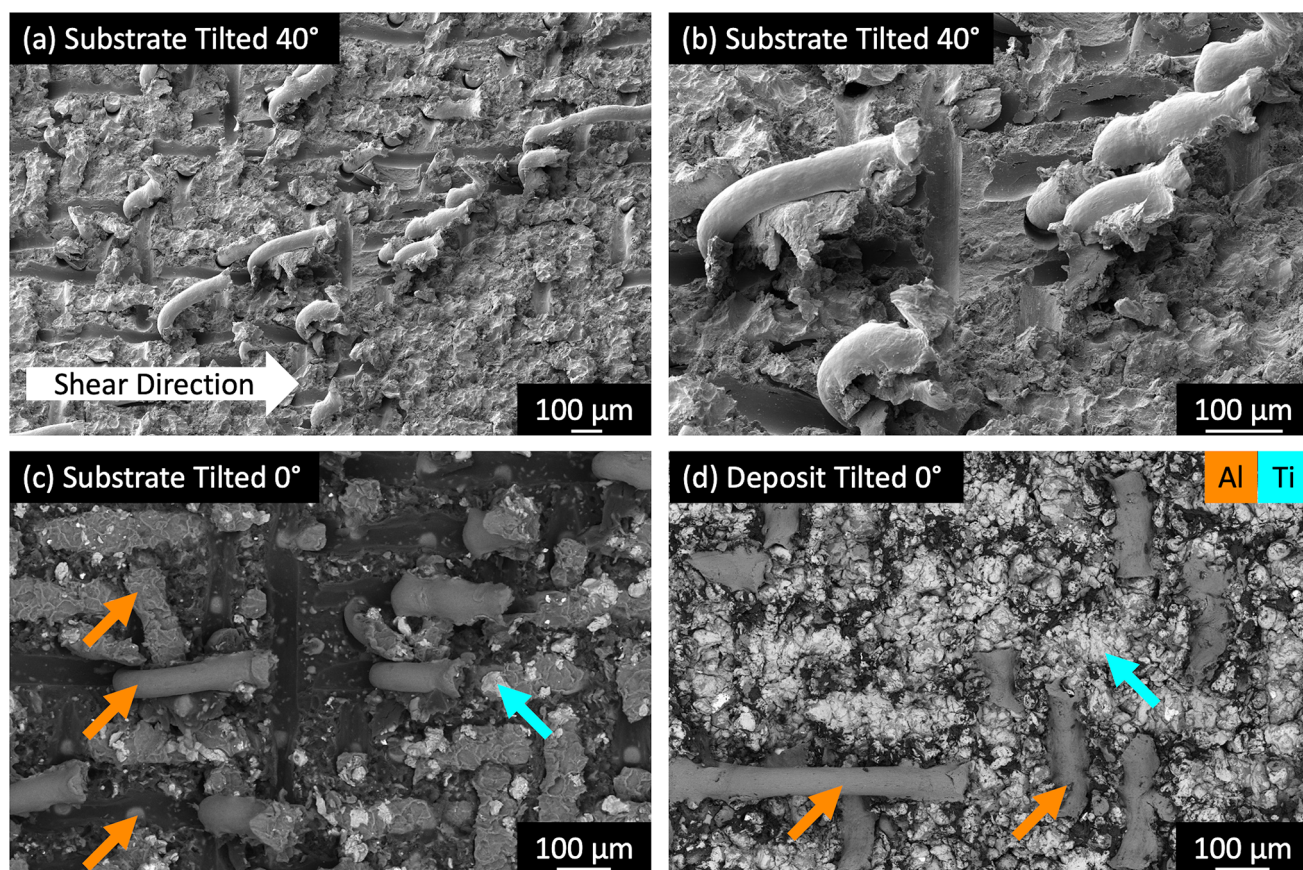
Fig. 11 (a, b) SE micrographs at 40° tilt and (c) BSE micrographs at 0° tilt of the substrate fracture surface. (d) BSE micrograph of the deposit fracture surface in plan view

deposit-substrate interface. With further refinement of BL designs, the proposed approach can be fully automated for both consistent application and rapid restoration of adherent leading-edge protection.

Conclusions

The effectiveness of the hybrid bond layer design for CS deposition onto CFRP was demonstrated. The mesh opening ratio (mesh opening size-to-powder diameter) determined the extent to which cold-sprayed powder mechanically interlocked and/or eroded epoxy exposed at mesh openings. Larger openings led to erosion of exposed adhesive, while smaller openings led to insufficient interlocking. The findings further indicated that as a general rule, mesh openings $> 10 \times$ the mean powder diameter or $< 1 \times$ the mean powder diameter are unlikely to result in acceptable mechanical interlocks for a continuous coating.

The design of the hybrid bond layer in conjunction with selection of powder diameter was major factors that controlled the microstructure of Ti deposits on CFRP. By incorporating an appropriately designed hybrid bond layer, cold-sprayed titanium, and possibly Ti-6Al-4 V, can be bonded to CFRP without adhesives. The process may be suitable for metallization of leading edges in air vehicles and of bearing surfaces in medical implants. The findings demonstrate an approach to expand applications of cold spray Ti alloys in protective coatings that can be restored, as well as in direct additive manufacturing onto composites.

References

1. P.-L. Feng, Y.-J. Cho, K. Kim, A. Blassino, I. Nault, S.-E. Lee and S. Nutt, Hybrid Bond Layers for Cold Spray Metallization of CFRP Surfaces, *J. Therm. Spray Technol.*, 2022 https://doi.org/10.1007/s11666-022-01478-x

2. A. Rezzoug, S. Abdi, A. Kaci and M. Yandouzi, Thermal Spray Metallisation of Carbon Fibre Reinforced Polymer Composites: Effect of Top Surface Modification on Coating Adhesion and Mechanical Properties, *Surf. Coat. Technol*, 2017, **2018**(333), p 13-23.

3. A. Rahimi, M. Hojjati, A. Dolatabadi and C. Moreau, Thermal Spray Coating on Polymeric Composite for De-Icing and Anti-Icing Applications, *J. Manuf. Sci. E. T. ASME*, 2021, **143**(10), p 1-9.

4. R. Melentiev, A. Yudhanto, R. Tao, T. Vuchkov and G. Lubineau, Metallization of Polymers and Composites: State-of-the-Art Approaches, *Mater. Des.*, 2022, **221**, p 110958. https://doi.org/10.1016/j.matdes.2022.110958

5. H. Parmar, F. Tucci, P. Carlone and T.S. Sudarshan, Metallisation of Polymers and Polymer Matrix Composites by Cold Spray: State of the Art and Research Perspectives, *Int. Mater. Rev.*, 2022, **67**(4), p 385-409.

6. R. Della Gatta, A.S. Perna, A. Viscusi, G. Pasquino and A. Astarita, Cold Spray Deposition of Metallic Coatings on Polymers: A Review, *J. Mater. Sci.*, 2022, **57**(1), p 27-57.

7. R. Melentiev, N. Yu and G. Lubineau, Polymer Metallization via Cold Spray Additive Manufacturing: A Review of Process Control Coating Qualities, and Prospective Applications, *Addit. Manuf.*, 2021, **48**(PB), p 102459. https://doi.org/10.1016/j.addma.2021.102459

8. A.C. Liberati, H. Che, M. Aghasibeig, K.R. Yu, P. Vo and S. Yue, On the Importance of Secondary Component Properties for Cold Spray Metallization of Carbon Fiber Reinforced Polymers, *J. Thermal Spray Technol.*, 2022, **31**(1-2), p 159-175.

9. J. Sun, K. Yamanaka, S. Zhou, H. Saito, Y. Ichikawa, K. Ogawa and A. Chiba, Adhesion Mechanism of Cold-Sprayed Sn Coatings on Carbon Fiber Reinforced Plastics, *Appl Surf Sci*, 2022, **579**, p 151873.

10. J. Sun, K. Yamanaka, S. Zhou, H. Saito, Y. Ichikawa, K. Ogawa and A. Chiba, Dynamic Recrystallization of Sn Coatings on Carbon-Fiber-Reinforced Plastics during Cold Spray Additive Manufacturing, *Addit Manuf*, 2022 https://doi.org/10.1016/j.addma.2022.102949

11. A.C. Liberati, H. Che, P. Fallah, P. Vo and S. Yue, Pull-off Testing and Electrical Conductivity of Sn-Based Metal Powder Mixtures Cold Sprayed on Carbon Fiber-Reinforced Polymers, *J. Thermal Spray Technol.*, 2022, **36**(3), p 1792-1812.

12. P. Feng, M.R. Rokni and S.R. Nutt, Depositing Aluminum onto PEKK Composites by Cold Spray, *J. Thermal Spray Technol.*, 2021, **30**(1-2), p 385-393.

13. V. Bortolussi, B. Figliuzzi, F. Willot, M. Faessel and M. Jeandin, Electrical Conductivity of Metal-Polymer Cold Spray Composite Coatings onto Carbon Fiber-Reinforced Polymer, *J. Therm. Spray Technol.*, 2020, **29**(4), p 642-656.

14. M.R. Rokni, P. Feng, C.A. Widener and S.R. Nutt, Depositing Al-Based Metallic Coatings onto Polymer Substrates by Cold Spray, *J. Thermal Spray Technol.*, 2019, **28**(7), p 1699-1708. https://doi.org/10.1007/s11666-019-00911-y

15. Y. Zou, Cold Spray Additive Manufacturing: Microstructure Evolution and Bonding Features, *Acc. Mater. Res.*, 2021, **2**(11), p 1071-1081.

16. W. Li, C. Cao and S. Yin, Solid-State Cold Spraying of Ti and Its Alloys: A Literature Review, *Prog Mater Sci*, 2018, **2020**(110), 100633.

17. M. Daroonparvar, A.K. Kasar, M.U.F. Khan, P.L. Menezes, C.M. Kay, M. Misra and R.K. Gupta, Improvement of Wear, Pitting Corrosion Resistance and Repassivation Ability of Mg-Based Alloys Using High Pressure Cold Sprayed (HPCS) Commercially Pure-Titanium Coatings, *Coatings*, 2021, **11**(1), p 1-20.

18. G. Zeng, S.H. Zahiri, S. Gulizia, Y. Chen, X.B. Chen and I. Cole, Hybrid Additive Manufacturing of Biocompatible Ti-Ta Composite Structures for Biomedical Applications, *J Mater Res*, 2021, **36**(18), p 3679-3690.

19. A. Vargas-Uscategui, P.C. King, S. Yang, C. Chu and J. Li, Toolpath Planning for Cold Spray Additively Manufactured Titanium Walls and Corners: Effect on Geometry and Porosity, *J Mater Process Technol*, 2021, **298**, p 1172723.

20. W. Żórawski, R. Molak, J. Mądry, J. Sienicki, A. Góral, M. Makrenek, M. Scendo and R. Dobosz, Experimental and Numerical Investigations of Titanium Deposition for Cold Spray Additive Manufacturing as a Function of Standoff Distance, *Materials*, 2021, **14**(19), p 5492.

21. F. Khodabakhshi, B. Marzbanrad, A. Yazdanmehr, H. Jahed and A.P. Gerlich, Tailoring the Residual Stress during Two-Step Cold Gas Spraying and Friction-Stir Surface Integration of Titanium Coating, *Surf Coat Technol*, 2019, **380**(October), p 125008.

22. P. Petrovskiy, A. Sova, M. Doubenskaia and I. Smurov, Influence of Hot Isostatic Pressing on Structure and Properties of Titanium Cold-Spray Deposits, *Int. J. Adv. Manuf. Technol.*, 2019, **102**(1-4), p 819-827.

23. C. Chen, Y. Xie, X. Yan, S. Yin, H. Fukanuma, R. Huang, R. Zhao, J. Wang, Z. Ren, M. Liu and H. Liao, Effect of Hot Isostatic Pressing (HIP) on Microstructure and Mechanical Properties of Ti6Al4V Alloy Fabricated by Cold Spray Additive Manufacturing, *Addit Manuf*, 2019, **27**(March), p 595-605.

24. J. Pattison, S. Celotto, R. Morgan, M. Bray and W. O'Neill, Cold Gas Dynamic Manufacturing: A Non-Thermal Approach to Freeform Fabrication, *Int. J. Mach. Tools Manuf.*, 2007, **47**(3-4), p 627-634.

25. S. Rahmati and B. Jodoin, Physically Based Finite Element Modeling Method to Predict Metallic Bonding in Cold Spray, *J. Thermal Spray Technol.*, 2020, **29**(4), p 611-629.

26. N.P. Zehtabi, A. Ardeshiri Lordejani, M. Guagliano and S. Bagherifard, Numerical Simulation of Cold Spray Bonding for CrFeNi Medium-Entropy Alloy, *Adv Eng Mater*, 2022, **2200603**, p 1-11.

27. G. Bae, Y. Xiong, S. Kumar, K. Kang and C. Lee, General Aspects of Interface Bonding in Kinetic Sprayed Coatings, *Acta Mater*, 2008, **56**(17), p 4858-4868.

28. S. Yin, X. Wang, X. Suo, H. Liao, Z. Guo, W. Li and C. Coddet, Deposition Behavior of Thermally Softened Copper Particles in Cold Spraying, *Acta Materialia*, 2013, **61**(14), p 5105-5118.

29. J. Zhou, K. Ma, C.X. Li, M. Yasir, X.T. Luo and C.J. Li, Microstructures of Aluminum Surfaces Reinforced with 316L Stainless Steel Particles via High-Speed Particle Injection and the Resulting Double-Strengthening Mechanism, *Surf. Coat. Technol.*, 2020, **385**(January), p 125380.

30. S. Yin, X. Suo, J. Su, Z. Guo, H. Liao and X. Wang, Effects of Substrate Hardness and Spray Angle on the Deposition Behavior of Cold-Sprayed Ti Particles, *J. Therm. Spray Technol.*, 2014, **23**(1-2), p 76-83.

31. K. Binder, J. Gottschalk, M. Kollenda, F. Gärtner and T. Klassen, Influence of Impact Angle and Gas Temperature on Mechanical Properties of Titanium Cold Spray Deposits, *J. Therm. Spray Technol.*, 2011, **20**(1-2), p 234-242.

32. K. Loke, Z.Q. Zhang, S. Narayanaswamy, P.K. Koh, V. Luzin, T. Gnaupel-Herold and A.S.M. Ang, Residual Stress Analysis of Cold Spray Coatings Sprayed at Angles Using Through-Thickness Neutron Diffraction Measurement, *J. Thermal Spray Technol.*, 2021, **30**(7), p 1810-1826.

33. D.H.L. Seng, Z.Z.Q. Zhang, Z.Z.Q. Zhang, T.L. Meng, S.L. Teo, B.H. Tan, Q. Loi and J. Pan, Influence of Spray Angle in Cold Spray Deposition of Ti-6Al-4V Coatings on Al6061-T6 Substrates, *Surf Coat Technol*, 2022, **432**(November), p 128068.

34. A. Fardan, C.C. Berndt and R. Ahmed, Numerical Modelling of Particle Impact and Residual Stresses in Cold Sprayed Coatings: A Review, *Surf Coat Technol*, 2021, **409**, p 126835.

35. Y. Ichikawa, R. Tokoro, M. Tanno and K. Ogawa, Elucidation of Cold-Spray Deposition Mechanism by Auger Electron Spectroscopic Evaluation of Bonding Interface Oxide Film, *Acta Material*, 2019, **164**, p 39-49.

36. M. Hassani, D. Veysset, Y. Sun, K.A. Nelson and C.A. Schuh, Microparticle Impact-Bonding Modes for Mismatched Metals: From Co-Deformation to Splatting and Penetration, *Acta Mater*, 2020, **199**, p 480-494. https://doi.org/10.1016/j.actamat.2020.08.038

37. X.L. Zhong, S.J. Haigh, X. Zhou and P.J. Withers, An In-Situ Method for Protecting Internal Cracks/Pores from Ion Beam Damage and Reducing Curtaining for TEM Sample Preparation Using FIB, *Ultramicroscopy*, 2020, **219**, p 113135.

38. R. Herring, K. Dyer, F. Martin and C. Ward, The Increasing Importance of Leading Edge Erosion and a Review of Existing Protection Solutions, *Renew Sustain Energy Rev*, 2019, **115**, p 109382.

39. R.J.K. Wood and P. Lu, Leading Edge Topography of Blades-a Critical Review, *Surf. Topogr. Metrol. Propert.*, 2021 https://doi.org/10.1088/2051-672X/abf81f

40. L. Mishnaevsky, C.B. Hasager, C. Bak, A.M. Tilg, J.I. Bech, S. Doagou Rad and S. Faester, Leading Edge Erosion of Wind Turbine Blades: Understanding, Prevention and Protection, *Renewable Energy*, 2021, **169**, p 953-969.

41. 3M, "Scotch-Weld Structural Adhesive Film AF191," 2009.

42. G.C. Murphy and B.J. Fuhrman, "Wide Chord Fan Blade," U.S. Patent and Trademark Office, 1992.

43. R.U.F. Gimat, M.A., Bassot, A.J.M., Jérémy, G.H., Mahieu, J.N. and Thibault, "Blade Comprising a Blade Body Made of Composite Material and a Leading-Edge Shield," U.S. Patent and Trademark Office, 2021.

44. D. Crall, C. Glynn, B. Busbey, J. Baldwin, and I. Prentice, "Adhesive Bonded Fan Blade," U.S. Patent and Trademark Office, 1998.

45. T.W.D. Kray, Nicholas Joseph, Dong-Jin Shim, "Metal Leading Edge Protective Strips for Airfoil COmponents and Method Therefor," U.S. Patent and Trademark Office, 2018.

46. S. Yin, P. He, H. Liao and X. Wang, Deposition Features of Ti Coating Using Irregular Powders in Cold Spray, *J. Therm. Spray Technol.*, 2014, **23**(6), p 984-990.

47. P. Kang, S.K. Youn and J.H. Lim, Modification of the Critical Projectile Diameter of Honeycomb Sandwich Panel Considering the Channeling Effect in Hypervelocity Impact, *Aerosp. Sci. Technol.*, 2013, **29**(1), p 413-425.

48. Shubham, C.S. Yerramalli, C. Sumant, R.K. Prusty, and B.C. Ray, Finite Element Modelling and Experimentation of Plain Weave Glass/Epoxy Composites under High Strain-Rate Compression Loading for Estimation of Johnson-Cook Model Parameters. Int J Impact Eng., https://doi.org/10.1016/j.ijimpeng.2022.104262 2022

49. S. Yin, X.F. Wang, W.Y. Li and H.E. Jie, Effect of Substrate Hardness on the Deformation Behavior of Subsequently Incident Particles in Cold Spraying, *Appl Surf Sci*, 2011, **257**(17), p 7560-7565.